

Research Article

Experimental Study on Dynamic Tensile Failure of Sandstone Specimens with Different Water Contents

Ming Li,¹ Gang Lin,² Wei Zhou ,³ Xianbiao Mao ,^{1,2} Lianying Zhang,⁴
and Rongrong Mao⁵

¹State Key Laboratory for Geomechanics and Deep Underground Engineering, China University of Mining and Technology, Xuzhou, Jiangsu 221116, China

²School of Mechanics and Civil Engineering, China University of Mining and Technology, Xuzhou, Jiangsu 221116, China

³School of Mines, China University of Mining and Technology, Xuzhou, Jiangsu 221116, China

⁴School of Civil Engineering, Xuzhou Institute of Technology, Xuzhou, Jiangsu 221018, China

⁵Department of Ship and Marine Engineering, Nantong Shipping College, Nantong, Jiangsu 226010, China

Correspondence should be addressed to Wei Zhou; loutian1982@126.com

Received 14 April 2019; Revised 23 July 2019; Accepted 30 July 2019; Published 9 September 2019

Academic Editor: Yuri S. Karinski

Copyright © 2019 Ming Li et al. This is an open access article distributed under the Creative Commons Attribution License, which permits unrestricted use, distribution, and reproduction in any medium, provided the original work is properly cited.

Understanding the effect of water saturation on dynamic failure of rocks is of great importance to tunnel excavation at water-rich coal mines and prevention of rock bursts by water injection. Dynamic Brazilian disc tests are performed to study mechanical behaviour of sandstones in this paper. The results indicate that water saturation significantly weakens the dynamic tensile strength of sandstones and increases the specimen strain at which the specimen fails. The damage degree of sandstones reduces gradually with increasing water contents. Failure of the sandstone specimen includes the crack initiation at the center of the specimen, macroscopic crack propagation, and stretch of the macroscopic crack through the specimen. In addition, parallel macroscopic crack propagation is found in the specimen with a low water content. From the observation of fracture sections, microstructures are compact in the specimen with high water contents. This is due to the swell of the kaolinite in the specimen after water saturation. The failure mechanism of microstructures is typical brittle failure in the specimen with a high water content, whereas ductile fracture is found in the specimen with a low water content. Different failure processes of microstructures lead to the differences between mechanical properties and macroscopic failure characteristics of the specimens with various water contents.

1. Introduction

Mechanical properties of coal and rock masses in underground coal mining are affected by many factors, such as water. For some water-rich deep tunnels, water contents of surrounding rock masses are relatively high. Part of the surrounding rock masses are even fully saturated [1]. Mechanical and physical properties of coal and rocks change remarkably in states of high water contents due to the existence of hydrophilic substances in these materials. This effect weakens the stability of surrounding rock masses and poses a challenge to tunnel support [2–4]. Besides geotechnical conditions, properties of coal and rock masses can also be influenced by tunnel excavation and coal mining that impose shock waves to the coal and rock

masses with high strain rates [5, 6]. The coal and rock masses under this condition exhibit totally different mechanical behaviour from that under dynamic loading. Understanding mechanical behaviour of coal and rock masses under the combined effects of high water contents and high strain rates is the prerequisite for controlling stability of surrounding rock masses of water-rich deep tunnels and parameter design of rock breaking by blasting or mechanical methods. Coal and rocks are more likely to fail in tension (compared with failure in compression). Disclosing mechanical characteristics of coal and rock materials under tension is of great importance for field applications. The investigation of this issue is also significant to prevention of dynamic hazards at coal mines by approaches, such as water injection [7].

Stability of geotechnical structures in the natural environment is sensitive to water, such as landslide caused by rainstorm [8] and collapse of underground space resulting from groundwater influx [9, 10]. Change of mechanical and physical properties of rocks under the effect of water (besides the dynamic effect of water) is the main cause of structure instability. Water saturation influences physical characteristics of rocks, such as increasing longitudinal wave velocities of rocks [11], swelling clay materials [12], and enhancing thermal conductivity of rocks, leading to variation of mechanical properties of rocks [13]. Erguler and Ulusay [14] found that uniaxial compressive strength (UCS), elastic moduli, and tensile moduli of clay rocks decrease notably as water content increases. Tang [15] noted that Poisson's ratio of the rock increases with a higher water content. Liu and Zhang [16] pointed out that water saturation decreases frictional angles of rock and soil and their cohesion changes nonmonotonously, following a Gaussian function. The variation of the internal structures due to water saturation is the root of the change of the mechanical and physical properties of rocks [17].

The rock is a heterogeneous, anisotropic, composite, and brittle material. Its tensile strength is much lower than the compressive strength. Therefore, failure of coal and rock masses in deep underground coal mining mainly depends on the tensile properties of the materials [18]. Reasonable specimen loading methods are the key to accurate measurement of tensile properties of rocks. Under static loading conditions, tension tests can be realized directly transforming the shape of the specimen, changing the size of the specimen, and utilizing special loading systems [19, 20]. However, for dynamic loading tests, it is difficult to apply the loading directly to the specimen. At present, performing Brazilian disc tests (an indirect tensile loading method) in split Hopkinson pressure bar (SHPB) systems is the most commonly used approach to studying dynamic tensile properties of rocks [21, 22]. Previous findings indicate that tensile strength of rocks increases with higher loading rates [23]. Recently, understanding dynamic tensile properties of rocks under special conditions has aroused great concerns, such as rocks after heat treatment, rocks eroded by chemical substances, and rocks cyclic loading and unloading. This also includes investigating dynamic tensile properties of rocks with different water contents [24–28]. Zhou et al. [29] carried out Brazilian disc tests on saturated sandstones with the SHPB system and concluded that tensile strength of the sandstone specimen decreases with a higher water content. Nevertheless, more efforts are still needed to disclose how water saturation influences tensile properties of rocks under dynamic loading conditions.

In this paper, Brazilian disc tests on sandstone specimens with different water contents are performed in the SHPB system with the purpose of understanding the effects of water saturation on dynamic tensile failure of the sandstone specimens. In addition, the scanning electron microscope (SEM) system is used to investigate the effect of water saturation on microstructure failure of sandstone specimens. The failure mechanism of sandstone specimens under dynamic tensile loading is studied.

2. Experimental Design and Procedures

2.1. Specimen Preparation and Experiment Scheme. The specimens in this study are collected from the roof stratum (sandstone) at the working face (about 1000 m in depth) at Jiahe Mine, China. The main composition of the specimen includes quartz (10.8%), kaolinite (11.6%), potash feldspar (4.5%), and anorthite (73.0%). A grinder is used to flatten the surface of each specimen end. The specimen has dimensions of 50 mm (in diameter) \times 25 mm (in height) with a disc shape. The experiment includes two main procedures: (1) prepare specimens with different water contents and (2) perform dynamic Brazilian disc tests in the SHPB system to study the effects of water saturation on the tensile characteristics of sandstone specimens at high strain rates.

The specimens are classified into four to five categories based on their water contents (included specimens that are fully saturated). Twenty specimens are prepared for each category.

2.2. Water Content Control. The method of controlling the water content of each specimen includes the following three procedures and is based on the International Society of Rock Mechanics (ISRM) standard: (1) completely dry the specimen, (2) saturate the specimen, and (3) dry the specimen to a specific water content.

An electrothermal constant-temperature drying oven (DHG9076 type) is used in the drying procedure (Figure 1(a)). First, the specimens are placed into the drying oven at a temperature of 108°C for 24 hours. Then, the specimens are taken out to measure their weight every 1 hour (the drying procedure is considered to be complete if the difference between the weight measured in two consecutive operations is less than 0.01 g). Finally, the specimens are cooled to room temperature and the weight of each specimen is measured (m_d).

Many methods of specimen saturation were used in previous studies. The vacuum pumping method is used in this study to saturate the specimens. A negative pressure vacuum pumping system is used (Figure 2). First, the specimens are placed into a sealed tank to be pumped in vacuum at a pressure of -0.09 MPa for 6 hours. Then, water is injected into the sealed tank until all the specimens are submerged. Finally, the specimens are pumped in vacuum at a pressure of -0.09 MPa for another 6 hours. Numerous bubbles overflow from the specimen surfaces at the early stage of saturation. The pressure inside of the sealed tank is set to atmospheric pressure once no bubble overflows from the specimen surfaces, and the specimens are kept in the sealed tank for 6 hours. After that, the specimens are weighted every 1 hour. The specimen is considered to be fully saturated (m_p) if the difference between the weight measured in two consecutive operations is less than 0.01 g.

The fully saturated specimens are again placed into the drying oven at a temperature of 50°C. The specimens are weighted every 10 minutes. The weight of each specimen in each operation is measured (m_h) to calculate the water content of the specimen. Five categories of water contents

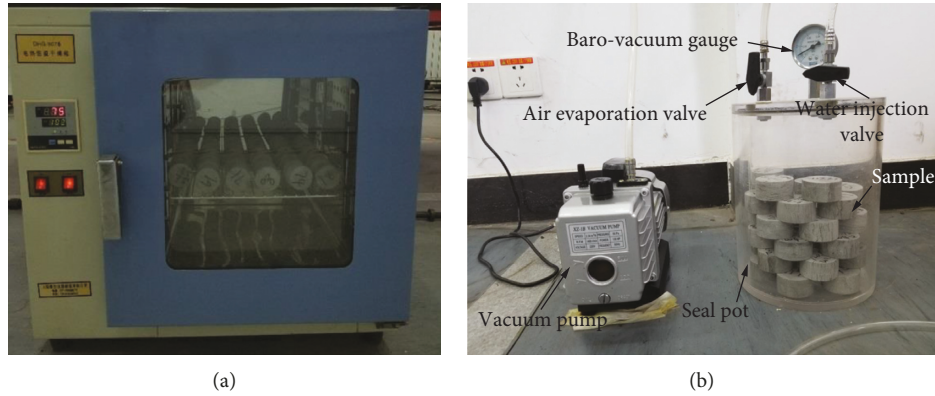


FIGURE 1: Specimen saturation system: (a) electrothermal drying oven; (b) negative pressure vacuum pumping system.

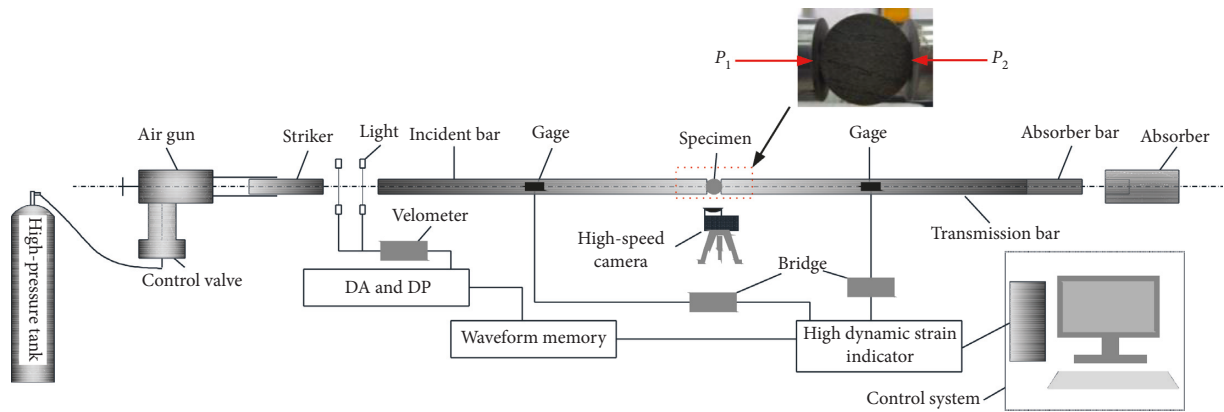


FIGURE 2: Dynamic Brazilian disc test in the split Hopkinson pressure bar system.

are determined, including $\omega_1 = 0.31\%$, $\omega_2 = 0.54\%$, $\omega_3 = 0.71\%$, $\omega_4 = 0.93\%$, and $\omega_5 = 1.09\%$ (fully saturated).

2.3. Dynamic Loading Test and Waveform. The dynamic Brazilian disc tests on sandstone specimens with different water contents in the SHPB system (Figure 2). Each test includes the following procedures: (1) clamp the specimen between the incident bar and the transmission bar, (2) pump high-pressure nitrogen into the incident bar to a given pressure magnitude, and (3) the striker is pushed by the high-pressure nitrogen to hit the incident bar in order to induce the stress wave loading. The stress wave propagates from the incident bar to the specimen and undergoes several times of reflection and refraction inside of the specimen until the specimen fails. The strain signals in the incident bar and the transmission bar in each test are collected by a dynamic strain collection system. The failure processes of the specimen are recorded by using a high-speed camera. Figures 3(a) and 3(b) show the waveform and the validation of the uniform stress assumption in the dynamic Brazilian disc test on the saturated sandstone specimen, respectively. The incident wave is almost a half-sine wave, and no obvious lateral oscillation is found (Figure 3(a)). The reflected wave has a similar shape to that of the incident wave. The amplitude of the transmitted wave is much lower than that of the incident wave and the

reflected wave (Figure 3(a)). The superimposition of the waveforms of the incident wave and the reflected wave is close to the waveform of the refraction wave (Figure 3(b)). Hence, the uniform stress assumption in the SHPB test is valid.

Numerous tests are performed on specimens with a given water content under an impact pressure ranging from 0.25 MPa to 0.35 MPa. This is to investigate how the mechanical characteristics of the specimens change against the water content at the same strain rate. Four strain rate conditions are determined (Table 1). The mean value ($\bar{\epsilon}$) of the strain rates ($\dot{\epsilon}$) in each test scenario (i.e., in which the tests have similar strain rates) is considered as the representative strain rate in the corresponding test scenario (e.g., tests ω_{1-1} , ω_{1-1} , ω_{1-1} , ω_{1-1} , and ω_{1-1} in Table 1 have a representative strain rate of 53.04).

3. Effect of Water Saturation on Mechanical Characteristics of Specimens in Dynamic Brazilian Disc Tests

3.1. Stress-Strain Curves of Sandstone Specimen in Dynamic Brazilian Disc Tests

(1) *Determination of Stress and Strain.* It is difficult to directly determine the stress-strain curve of the specimen from the dynamic Brazilian disc test. An

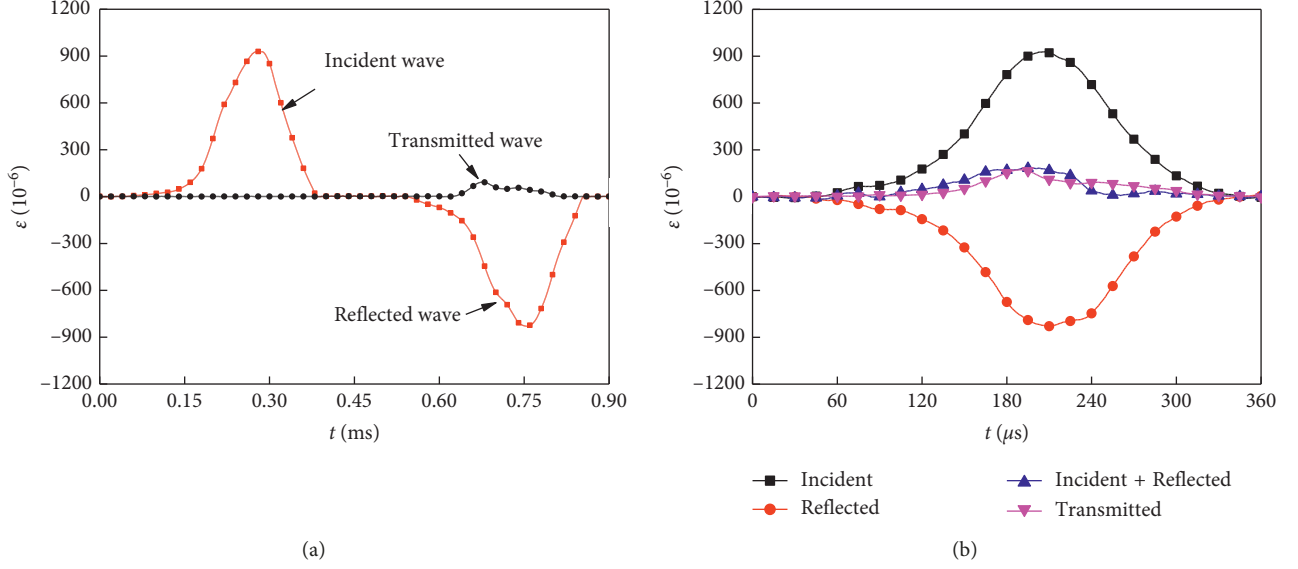


FIGURE 3: Dynamic tensile tests on sandstone specimens: (a) waveforms; (b) validation of the uniform stress assumption.

TABLE 1: Loading strain rates of specimens with different water contents.

| No. | ω (%) | $\dot{\varepsilon}$ (s^{-1}) | $\tilde{\varepsilon}$ (s^{-1}) |
|----------------|--------------|----------------------------------|------------------------------------|
| ω_{1-1} | 0.31 | 53.12 | |
| ω_{2-1} | 0.54 | 53.80 | |
| ω_{3-1} | 0.71 | 52.38 | 53.04 |
| ω_{4-1} | 0.93 | 53.12 | |
| ω_{5-1} | 1.09 | 52.79 | |
| ω_{1-3} | 0.31 | 89.64 | |
| ω_{2-3} | 0.54 | 88.70 | |
| ω_{3-3} | 0.71 | 89.81 | 89.04 |
| ω_{4-3} | 0.93 | 88.69 | |
| ω_{5-3} | 1.09 | 88.37 | |
| ω_{1-2} | 0.31 | 73.28 | |
| ω_{2-2} | 0.54 | 72.88 | |
| ω_{3-2} | 0.71 | 73.64 | 73.16 |
| ω_{4-2} | 0.93 | 73.05 | |
| ω_{5-2} | 1.09 | 72.93 | |
| ω_{1-4} | 0.31 | 105.20 | |
| ω_{2-4} | 0.54 | 104.46 | |
| ω_{3-4} | 0.71 | 105.47 | 104.87 |
| ω_{4-4} | 0.93 | 104.44 | |
| ω_{5-4} | 1.09 | 104.78 | |

indirect method is used to derive the stress-strain relationship, using the tensile stress at the center of the specimen and the axial deformation of the specimen.

The tensile stress at the center of the specimen is calculated by using equation (1) based on the method used in the static Brazilian disc test:

$$\sigma(t) = \frac{P_1(t) + P_2(t)}{\pi DB}, \quad (1)$$

where $\sigma(t)$ is the stress at the center of the specimen, $P_1(t)$ and $P_2(t)$ are the loading forces applying to the specimen ends, D is the specimen diameter (50 mm), and B is the specimen thickness (25 mm).

Equation (2) is used to calculate $P_1(t)$ and $P_2(t)$ based on the elastic wave theory:

$$\begin{cases} P_1(t) = AE_B[\varepsilon_i(t) + \varepsilon_r(t)], \\ P_2(t) = AE_B\varepsilon_t(t), \end{cases} \quad (2)$$

where A is the diameter of the incident bar, E_B is the elastic modulus of the incident bar, and $\varepsilon_i(t)$, $\varepsilon_r(t)$, and $\varepsilon_t(t)$ are the strain signals of the incident wave, reflected wave, and transmitted wave in the incident bar, respectively.

Based on the uniform stress assumption, the following equation is derived:

$$\varepsilon_i(t) + \varepsilon_r(t) = \varepsilon_t(t). \quad (3)$$

Substitute equation (3) into equation (2):

$$P_1(t) = P_2(t) = AE_B\varepsilon_t(t). \quad (4)$$

The tensile stress at the center of the specimen at a given time can be estimated if equation (4) is substituted into equation (1).

The change of the specimen diameter in the loading direction (δ_D) can be calculated by the three-wave method. The axial relative strain of the specimen in the loading direction (ε_D) can be calculated by using the following equation:

$$\varepsilon_D = \frac{\delta_D}{D}. \quad (5)$$

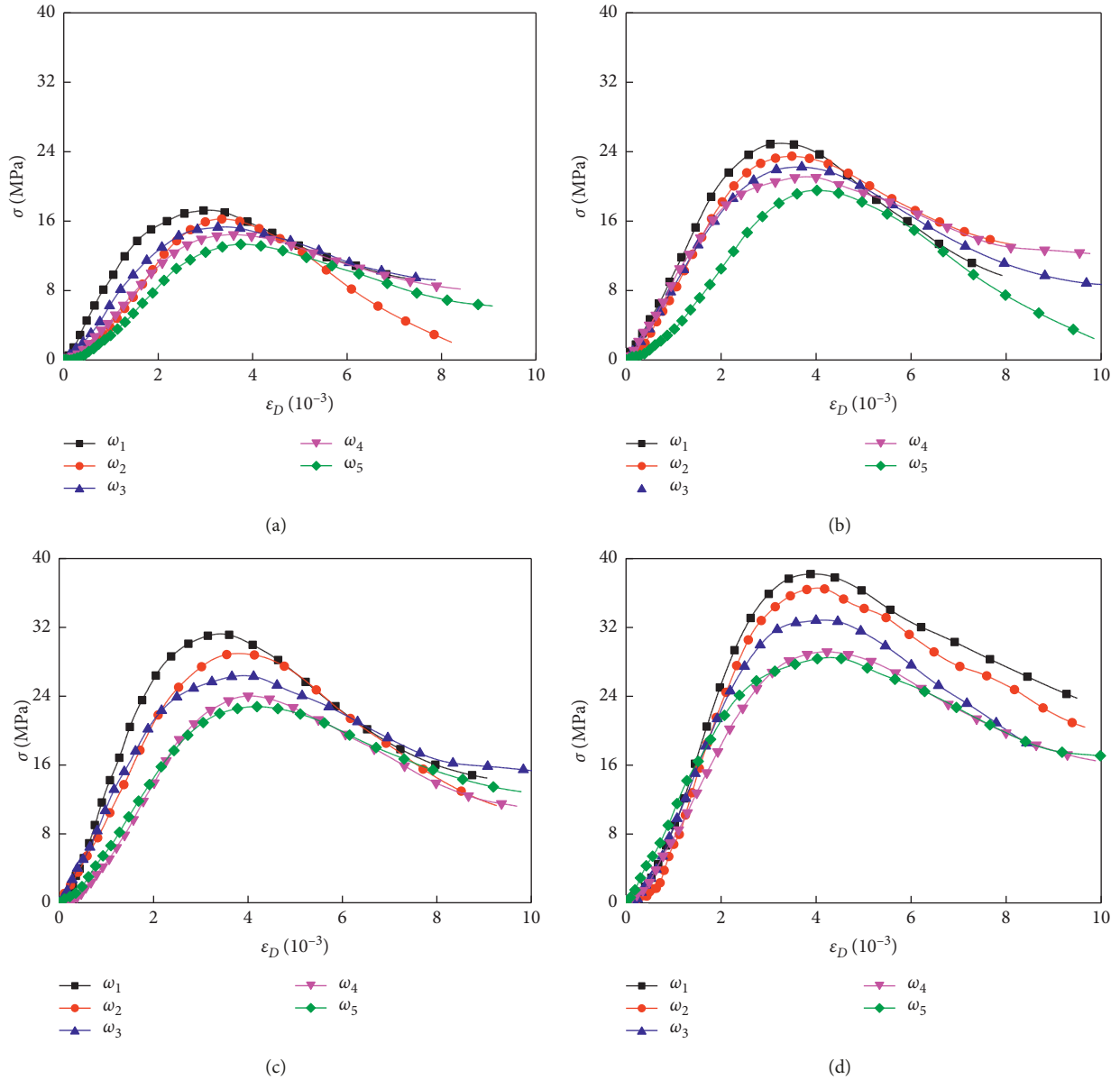


FIGURE 4: Stress-strain curves of sandstone specimens with different water contents: at a strain rate of (a) 53.04 s^{-1} , (b) 73.16 s^{-1} , (c) 89.04 s^{-1} , and (d) 104.87 s^{-1} .

Finally, the stress-strain relationship of the sandstone specimen in the dynamic Brazilian disc test can be obtained based on equations (1) and (5).

- (2) *Characteristics of Stress-Strain Curves.* The stress-strain curves of sandstone specimens with different water contents in the dynamic Brazilian disc tests at various strain rates are presented in Figure 4. For a given strain rate, the stress-strain curves of the specimens with different water contents are similar to each other. The tensile failure processes can be divided into four stages, including compaction, linear elastic deformation, nonlinear plastic deformation (due to microcrack propagation), and the postfailure stage. For a given strain rate, the compaction stage becomes more obvious and the relative strain increases with the

increasing water content. The reason is that the water weakens the kaolinite in the specimen, which enhances the compressibility between the kaolinite grains. The slope of the stress-strain curve in the elastic deformation stage decreases with an increasing water content. In addition, water saturation influences other mechanical properties of the sandstone specimens, such as the tensile strength (σ_{wt}) and the strain at which the specimen fails (ϵ_{Dt}).

3.2. Variation of Dynamic Tensile Strength of Sandstone Specimens. The tensile strength of all the sandstone specimens is listed in Table 2. The tensile strength of the specimens with different water contents at a given strain rate is compared in Figure 5. For a given strain rate, the tensile strength of the

TABLE 2: Change of the tensile strength of the specimens against the water contents.

| No. | $\dot{\epsilon}$ (s^{-1}) | ω (%) | $\sigma_{\omega t}$ (MPa) |
|----------------|-------------------------------|--------------|---------------------------|
| ω_{1-1} | 53.04 | 0.31 | 5.75 |
| ω_{2-1} | | 0.54 | 5.41 |
| ω_{3-1} | | 0.71 | 5.11 |
| ω_{4-1} | | 0.93 | 4.82 |
| ω_{5-1} | | 1.09 | 4.44 |
| ω_{1-3} | 89.04 | 0.31 | 10.41 |
| ω_{2-3} | | 0.54 | 9.65 |
| ω_{3-3} | | 0.71 | 8.80 |
| ω_{4-3} | | 0.93 | 8.01 |
| ω_{5-3} | | 1.09 | 7.60 |
| ω_{1-2} | 73.16 | 0.31 | 8.32 |
| ω_{2-2} | | 0.54 | 7.83 |
| ω_{3-2} | | 0.71 | 7.41 |
| ω_{4-2} | | 0.93 | 7.04 |
| ω_{5-2} | | 1.09 | 6.51 |
| ω_{1-4} | 104.87 | 0.31 | 12.73 |
| ω_{2-4} | | 0.54 | 12.19 |
| ω_{3-4} | | 0.71 | 10.95 |
| ω_{4-4} | | 0.93 | 9.73 |
| ω_{5-4} | | 1.09 | 9.50 |

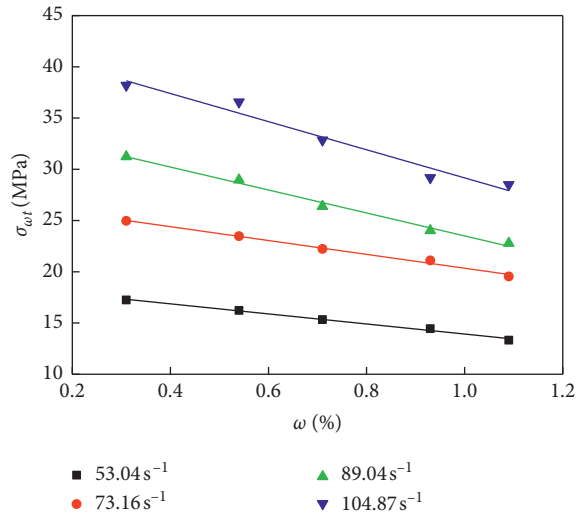


FIGURE 5: Change of the tensile strength against the water content.

specimens decreases almost linearly as the water content increases. For the four strain rates considered in this study ($\dot{\epsilon} = 53.04 s^{-1}$, $73.16 s^{-1}$, $89.04 s^{-1}$, and $104.87 s^{-1}$), the tensile strength decreases from 5.75 MPa, 8.32 MPa, 10.41 MPa, and 12.73 MPa to 4.44 MPa (by 22.78%), 6.51 MPa (by 21.80%), 7.06 MPa (by 26.99%), and 9.50 MPa (by 25.39%), respectively, if the water content increases from 0.31% to 1.09%. The water in the specimen leads to the swelling and weakening of kaolinite composition. This reduces the frictional force between particles and weakens the deformability of the specimen.

The relationship between the tensile strength and the water content can be described by using the following equation based on the results in Figure 5, using liner fitting:

$$\sigma_{\omega t} = k\omega + \sigma_{0t}, \quad (6)$$

TABLE 3: Relationship between tensile strength and the water contents at different strain rates.

| Parameter | $\dot{\epsilon}$ (s^{-1}) | | | |
|---------------|-------------------------------|-------|-------|--------|
| | 53.04 | 73.16 | 89.04 | 104.87 |
| k | -1.64 | -2.25 | -3.74 | -4.58 |
| σ_{0t} | 6.28 | 9.03 | 11.57 | 14.30 |

where k is the slope in the linear fitting and σ_{0t} is the intercept (which equals to the tensile strength of the specimen in a completely dry condition).

The regression coefficients in equation (6) (i.e., k and σ_{0t}) at different strain rates are given in Table 3. The absolute value of k increases gradually with an increasing strain rate. This suggests that the tensile strength of the specimen becomes more sensitive to the water content as the strain rate increases.

4. Effect of Different Water Contents on Dynamic Tensile Failure of Specimens

4.1. Dynamic Tensile Failure Processes of Specimens. A high-speed camera (Phantom v611 type) is used to record the dynamic tensile failure processes of the sandstone specimens. The initiation and propagation of macroscopic cracks at different loading time are studied. Figures 6 and 7 provide the dynamic failure processes of the sandstone specimens at a strain rate of $89.04 s^{-1}$ with water contents of 0.31% and 1.09%, respectively. The failure processes of the specimen with a water content of 0.31% included (Figure 6) crack initiation at the center of the specimen ($t = 55 \mu s$), macroscopic crack propagation; development of parallel cracks ($t = 165 \mu s$), macroscopic cracks stretch through the specimen ($t = 275 \mu s$), and specimen failure ($t = 605 \mu s$). The failure processes of the specimen with a water content of 1.09% included (Figure 7) crack initiation at the center of the specimen ($t = 55 \mu s$), quick macroscopic crack propagation, formation of stress concentration areas around the loading ends ($t = 275 \mu s$), macroscopic cracks stretch through the specimen ($t = 440 \mu s$), and specimen failure ($t = 605 \mu s$).

4.2. Failure Processes of Specimens with Different Water Contents. The similarities of the failure processes of the specimens with different water contents (0.31% and 1.09%) in Figures 6 and 7 are summarized as follows. Crack initiation occurs at the center of the specimen, and the macroscopic cracks propagate along the loading direction. In addition, obvious stress concentration areas are found around the loading ends. All of these similarities are related to the stress distribution in the specimen.

Two main differences exist in the failure processes in Figures 6 and 7. The macroscopic crack propagates and stretches through the specimen, leading to the failure of the specimen with a higher water content (1.09%), whereas parallel macroscopic cracks develop and propagate in the specimen with a lower water content (0.31%), resulting in the ultimate failure of the specimen. The reason is that the hydrophilic

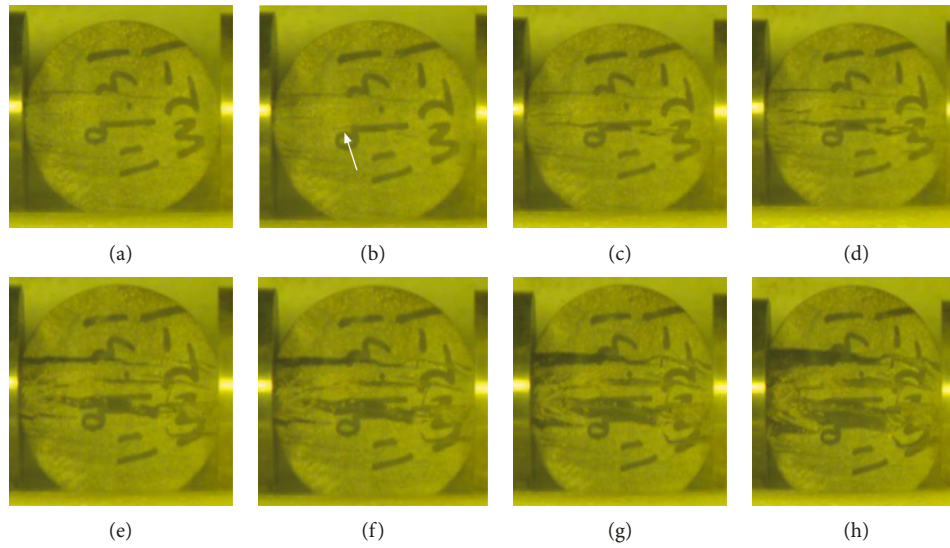


FIGURE 6: Failure processes of the specimen with a water content of 0.31%: (a) $t = 0 \mu\text{s}$; (b) $t = 55 \mu\text{s}$; (c) $t = 110 \mu\text{s}$; (d) $t = 165 \mu\text{s}$; (e) $t = 275 \mu\text{s}$; (f) $t = 330 \mu\text{s}$; (g) $t = 440 \mu\text{s}$; (h) $t = 605 \mu\text{s}$.

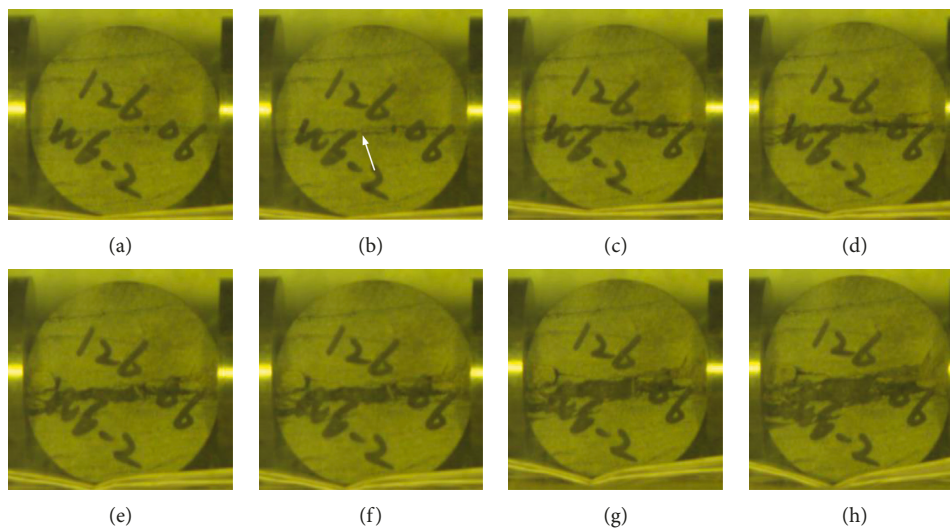


FIGURE 7: Failure processes of the specimen with a water content of 1.09%: (a) $t = 0 \mu\text{s}$; (b) $t = 55 \mu\text{s}$; (c) $t = 110 \mu\text{s}$; (d) $t = 165 \mu\text{s}$; (e) $t = 275 \mu\text{s}$; (f) $t = 330 \mu\text{s}$; (g) $t = 440 \mu\text{s}$; (h) $t = 605 \mu\text{s}$.

substances in the sandstone, such as the kaolinite, dehydrate when the water content is relatively low (0.31%). This leads to the formation of numerous microcracks between the particles. Hence, multiple macroscopic cracks develop and propagate in the loading process. On the contrary, the hydrophilic substances absorb water and swell in the specimen with a relatively high water content (1.09%). Less microcracks contribute to the formation of macroscopic cracks if the specimen is loaded at a higher strain rate. Besides, the shapes of the fragments of the two ruptured specimens are clearly different. This is due to the different forms of macroscopic crack propagation in these two specimens.

4.3. Failure Characteristics of Specimens with Different Water Contents. The fragments of all the specimens are presented in Figures 8, 9, 10, and 11. For a given strain rate, the amount

of the fragments reduces gradually if the specimen has higher water contents. When a specimen with a relatively low water content ruptures, some small spalls are found besides a large fragment with a semicircle cross section (the volume of which is about half of the specimen). The amount of the small spalls decreases once the water content increases to 1.09%. The fragments of the ruptured specimen are consistent with that in the static Brazilian disc test, which include two similar large fragments with semicircular cross sections.

A classifying screen is used to categorize the fragments based their grain sizes. Seven categories are determined according to the range of the grain size, including 0 to 2.5 mm, 2.5 to 5.0 mm, 5.0 to 8.0 mm, 8.0 to 12.0 mm, 12.0 to 15.0 mm, 15.0 to 20.0 mm, and 20.0 to 50.0 mm. These categories are numbered 1 to 7, respectively (e.g., the

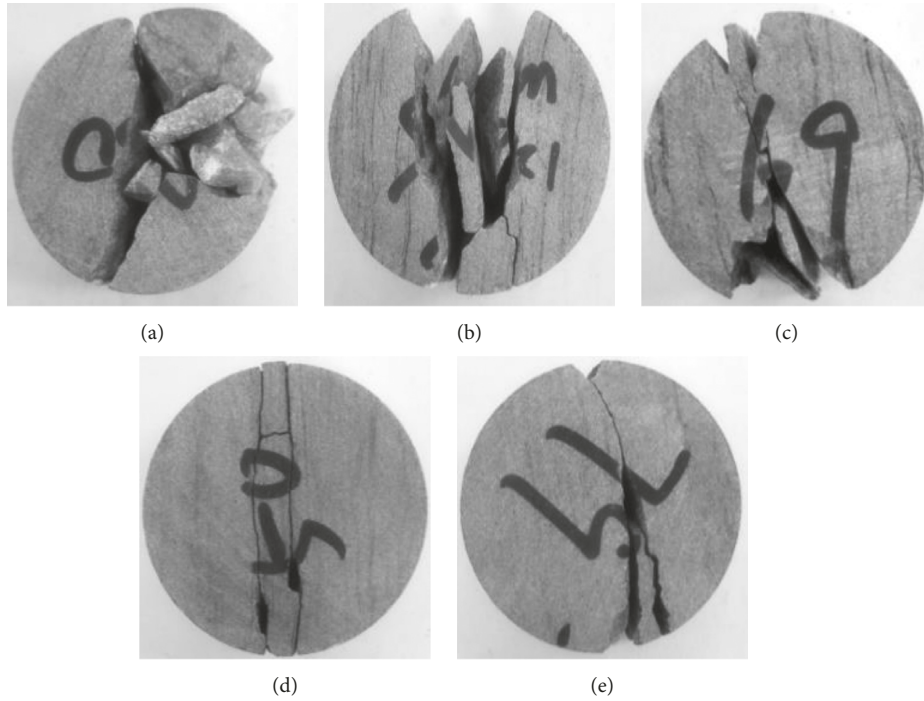


FIGURE 8: Failure of specimens with different water contents at a strain rate of 53.04 s^{-1} : (a) $\omega = 0.31\%$; (b) $\omega = 0.54\%$; (c) $\omega = 0.71\%$; (d) $\omega = 0.93\%$; (e) $\omega = 1.09\%$.

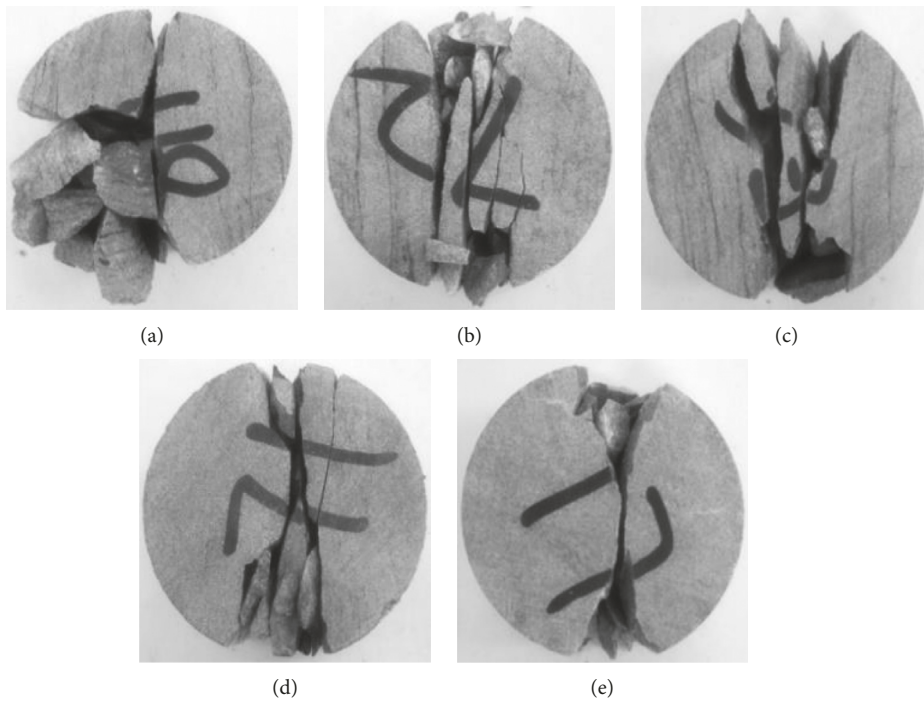


FIGURE 9: Failure of specimens with different water contents at a strain rate of 73.16 s^{-1} : (a) $\omega = 0.31\%$; (b) $\omega = 0.54\%$; (c) $\omega = 0.71\%$; (d) $\omega = 0.93\%$; (e) $\omega = 1.09\%$.

smallest size (0 to 2.5 mm) is numbered 1 and the largest size (20.0 to 50.0 mm) is numbered 7). The damage degree of the specimen is evaluated by using the following equation:

$$\delta = \sum_{i=1}^7 m_{iv} d_{iv}, \quad i = 1, 2, \dots, 7, \quad (7)$$

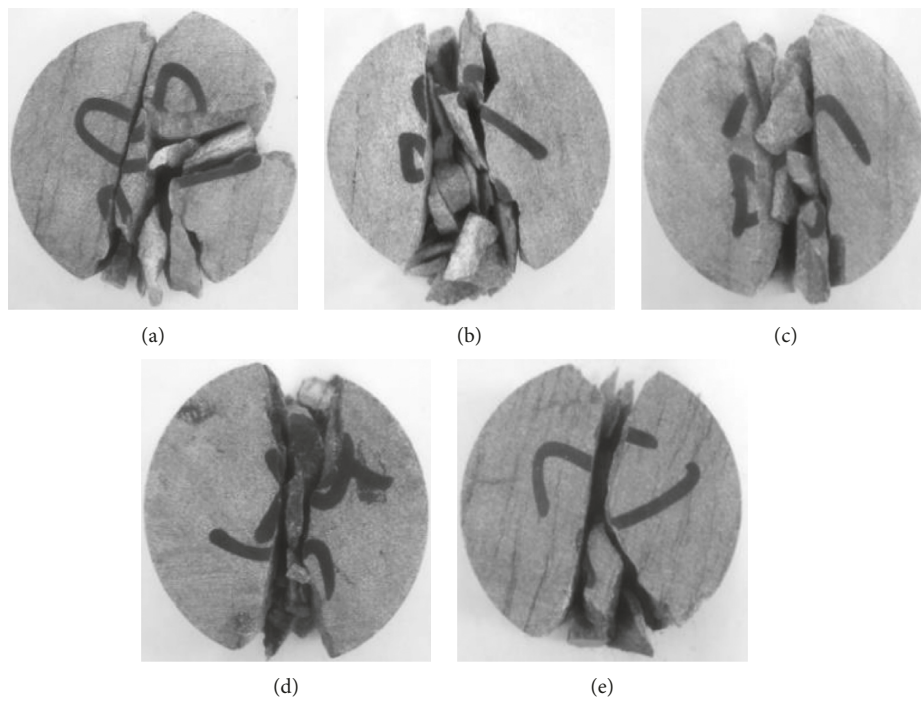


FIGURE 10: Failure of specimens with different water contents at a strain rate of 89.04 s^{-1} : (a) $\omega = 0.31\%$; (b) $\omega = 0.54\%$; (c) $\omega = 0.71\%$; (d) $\omega = 0.93\%$; (e) $\omega = 1.09\%$.

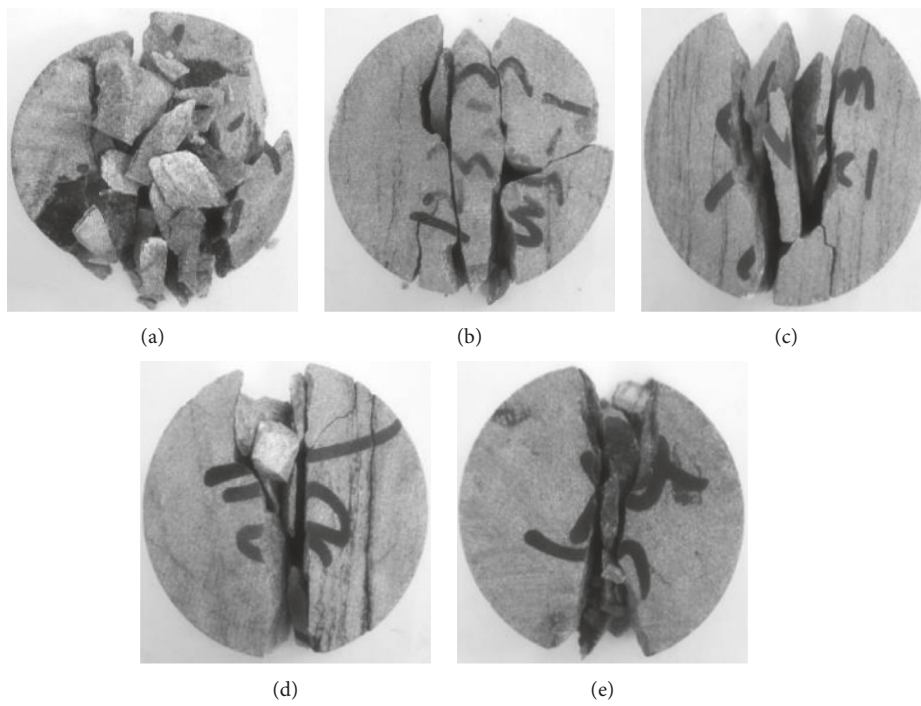


FIGURE 11: Failure of specimens with different water contents at a strain rate of 104.87 s^{-1} : (a) $\omega = 0.31\%$; (b) $\omega = 0.54\%$; (c) $\omega = 0.71\%$; (d) $\omega = 0.93\%$; (e) $\omega = 1.09\%$.

TABLE 4: Average grain sizes of all the specimens.

| $\dot{\epsilon}$ (s^{-1}) | δ (mm) | | | | |
|-------------------------------|-------------------|-------------------|-------------------|-------------------|-------------------|
| | $\omega = 0.31\%$ | $\omega = 0.54\%$ | $\omega = 0.71\%$ | $\omega = 0.93\%$ | $\omega = 1.09\%$ |
| 53.04 | 18.45 | 19.21 | 20.43 | 22.54 | 24.12 |
| 73.16 | 17.12 | 18.13 | 19.42 | 21.33 | 23.25 |
| 89.04 | 16.02 | 17.25 | 18.36 | 20.08 | 22.11 |
| 104.87 | 14.33 | 16.27 | 17.41 | 18.72 | 20.67 |

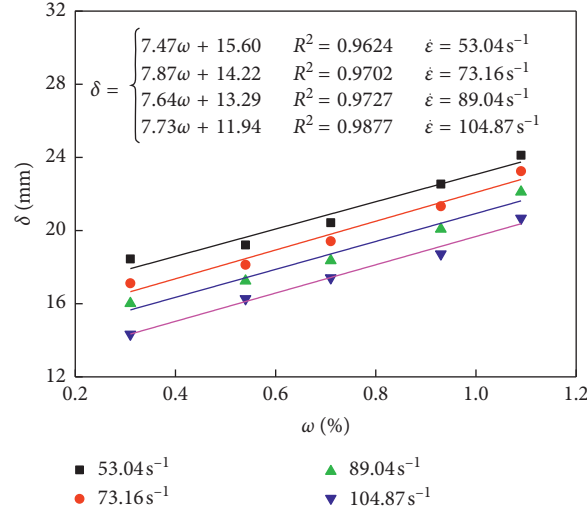


FIGURE 12: Change of the average grain size against the water content.

where δ is the average grain size of the ruptured specimen, i is the category number, m_{iv} is the ratio of the weight of the i th category fragments to the overall weight of the fragments, and d_{iv} is the average grain size in the i th category (the average of the largest grain size and the smallest grain size in the i th category).

Table 4 lists the average grain sizes (calculated by using equation (7)) of all the specimens. Figure 12 shows the change of the average grain size against the water content at various strain rates. For a given strain rate, the average grain size increases gradually in a linear tendency with an increasing water content. This suggests that the damage degree of the sandstone specimen also decreases gradually. The average grain sizes at different strain rates increase by 30.73% ($\dot{\epsilon} = 53.04 s^{-1}$), 35.81% ($\dot{\epsilon} = 73.16 s^{-1}$), 38.02% ($\dot{\epsilon} = 89.04 s^{-1}$), and 44.24% ($\dot{\epsilon} = 104.87 s^{-1}$), respectively, when the water content increases from 0.31% to 1.09%. The slopes of the linear fitting lines in Figure 12 (reflecting the relationship between the average grain size and the water content) are close to each other. This indicates that the strain rate has limited influence on the change of the average grain size against the water content.

5. Dynamic Failure of Microstructures in Sandstone Specimens with Different Water Contents

The SEM system (TESCAN VEGA3 type) is used to observe the fracture sections of sandstone specimens with different

water contents. The fracture sections in Figure 13 are mechanically cut from the intact specimens (that are not loaded by the SPHB system). The fracture sections in Figure 14 are obtained from the specimens with different water contents loaded at a strain rate of $89.04 s^{-1}$. The fracture sections in Figure 13 show that a certain amount of microcracks and pores exists in the specimens that are completely dry or have relatively low water contents. Microstructures become compact as the water content increases. No visible defect is found once the specimen is fully saturated. The reasons for the differences observed in Figure 13 are discussed as follows. The water in the specimen evaporates in the drying process. The clay materials, such as the kaolinite, dehydrate and shrink, leading to the fracture of the bonded materials between the particles and the formation of microcracks and pores. The clay materials absorb water and swell once the water content increases and completely fill the defects formed in the drying process.

Figure 14 provides the fracture sections of the specimens with different water contents loaded at a high strain rate ($89.04 s^{-1}$) at two magnifications (50 times and 2000 times). The fracture sections observed at a magnification of 50 look rough, and numerous convex particles are found. With the increase of the water content, the fracture sections become flat and the convex particles gradually disappear. The fracture sections observed at a magnification of 2000 notably differ from each other. Visible dimples and slip separation are found in the specimens with relatively low water contents ($\omega = 0.31\%$ and 0.54%), whereas intergranular cracks, cleavage steps, and single grains are observed in the

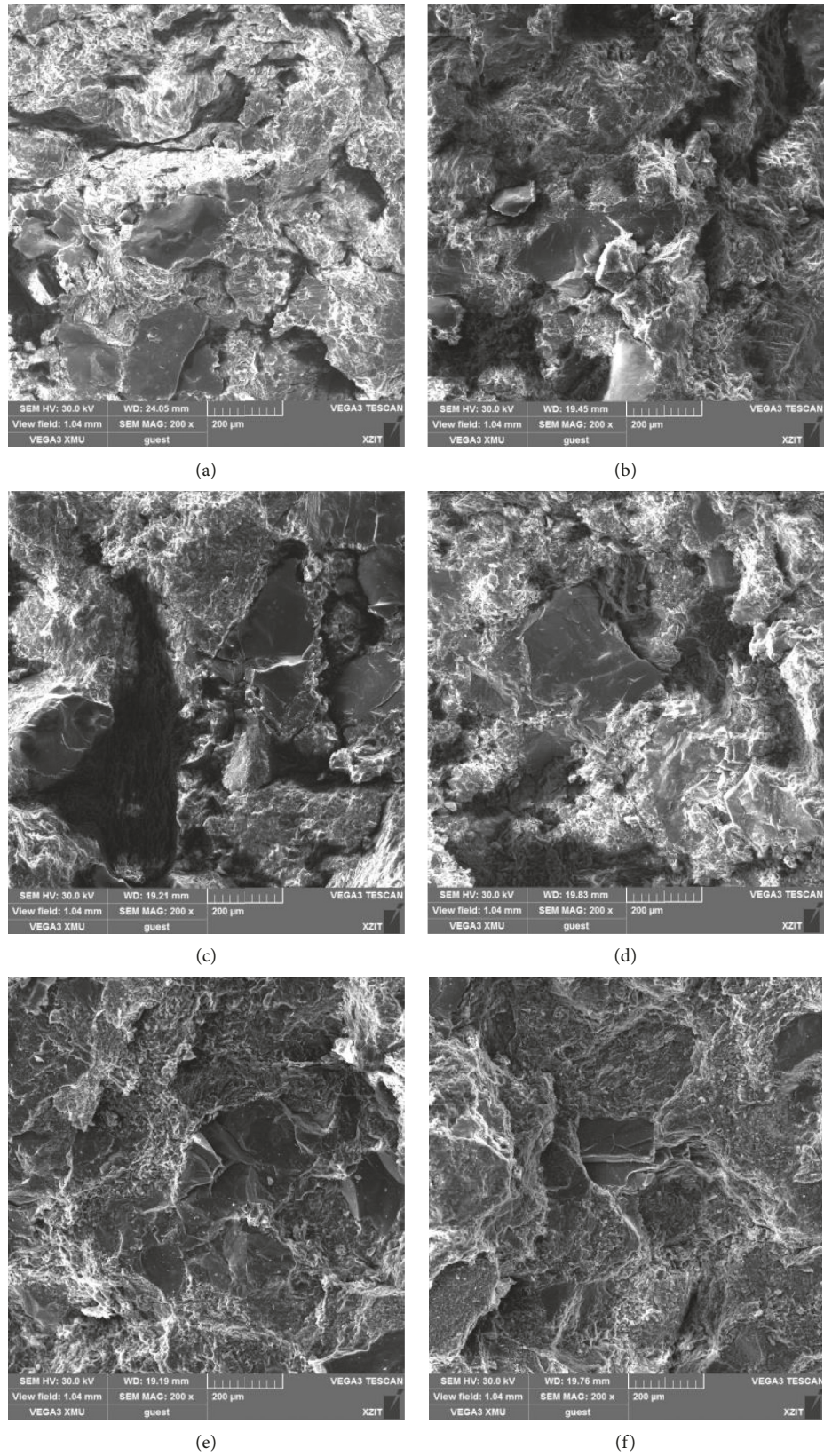
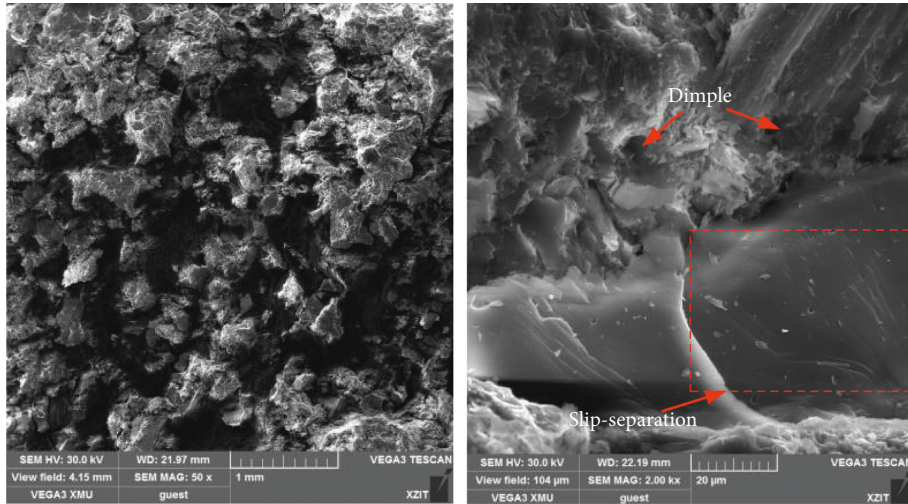
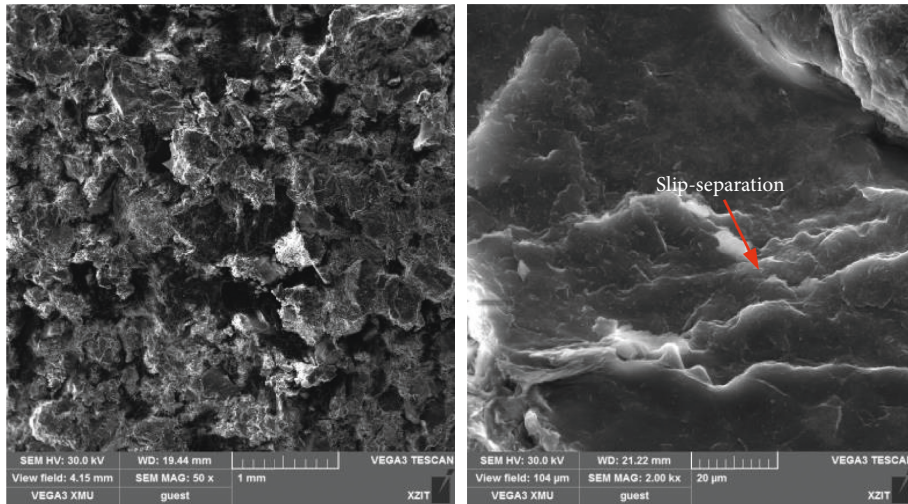


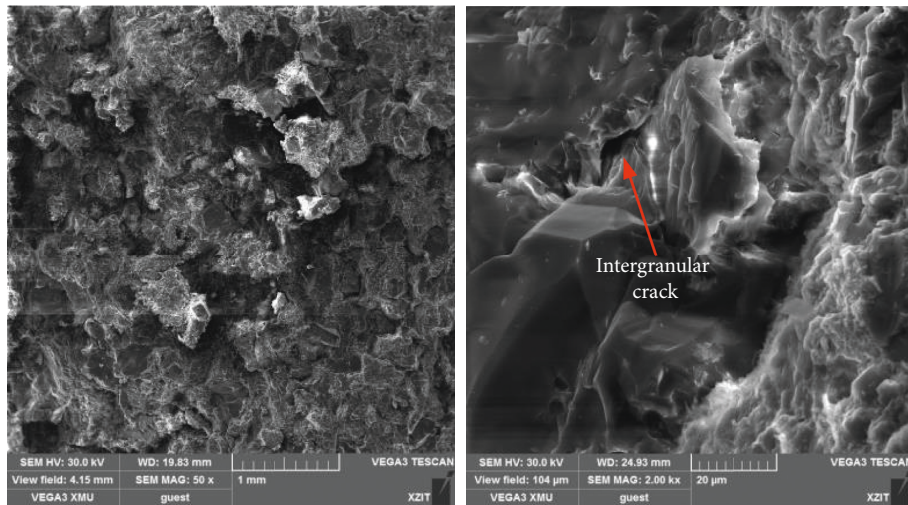
FIGURE 13: Fracture sections of specimens with different water contents: (a) $\omega = 0.00\%$; (b) $\omega = 0.31\%$; (c) $\omega = 0.54\%$; (d) $\omega = 0.71\%$; (e) $\omega = 0.93\%$; (f) $\omega = 1.09\%$.



(a)



(b)



(c)

FIGURE 14: Continued.

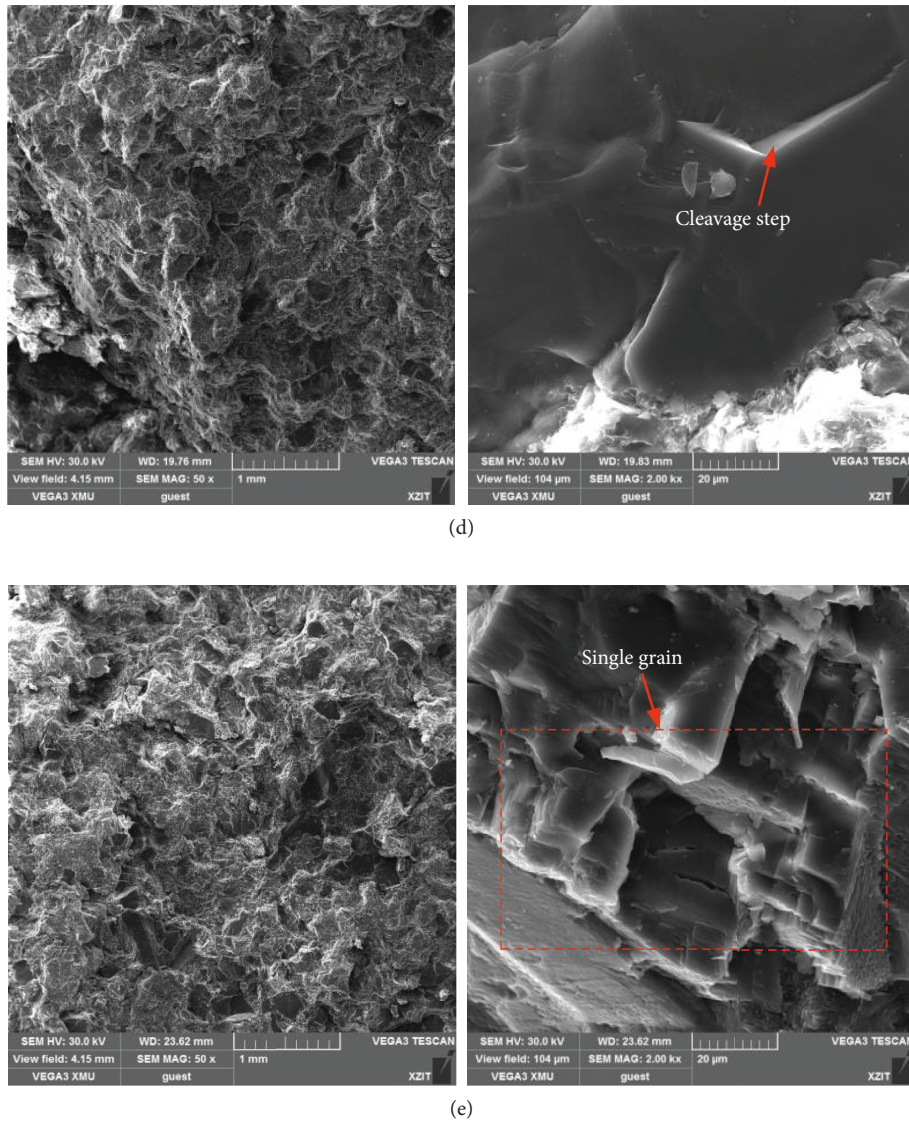


FIGURE 14: Failure of microstructures in specimens with different water contents: (a) $\omega = 0.31\%$; (b) $\omega = 0.54\%$; (c) $\omega = 0.71\%$; (d) $\omega = 0.93\%$; (e) $\omega = 1.09\%$.

specimens with relatively high water contents ($\omega = 0.71\%$, 0.93% , and 1.09%). The specimens with relatively high water contents contain more microcracks and pores (compared with that with relatively low water contents), and hence, more defects contribute to the failure of the specimens. This leads to smaller average grain sizes of the specimens and more serious macroscopic damage. Moreover, the fracture sections become more complex and uneven. The dehydration and shrinkage of the clay materials result in more frictional resistance to specimen failure. This leads to a higher macroscopic load-bearing ability of the specimen and more serious specimen damage. Meanwhile, the friction between the particles induces more plastic deformation in the specimen. Hence, ductile fracture is found in the fracture sections. When the specimens with relatively high water contents are loaded at high strain rates, the propagation of the microcracks is fast and leads to the failure of the specimens. In this case, the fracture sections are more flat

and the failure of the microstructures is mainly the brittle fracture that consumes less energy.

6. Conclusions

Dynamic Brazilian disc tests are performed on sandstone specimens with different water contents in the split Hopkinson pressure bar system in this paper. The failure processes and microstructure failure in the sandstone specimens with different water contents are observed by using a high-speed camera and the scanning electron microscope system, respectively. The results of dynamic Brazilian disc tests show that, under a given strain rate, both the specimen strain at which the compaction stage ends and the specimen strain at which the specimen fails increase with a higher water content, whereas the tensile strength reduces in a linear tendency as the water content increases. Meanwhile, the tensile strength of the specimen becomes more sensitive to

the water content at a higher strain rate. Dynamic failure process shows that specimens with different water content have to undergo three stages: crack initiation at the center of the specimen; macroscopic crack propagation; and finally, the stretch of macroscopic crack through the specimen. In the specimen with a low water content, parallel macroscopic cracks form and propagate, leading to more complex failure processes of the specimen, but in specimens with the high water content, it is opposite, obvious stress concentration areas are observed around the loading ends. The characteristics of the fragments after the specimen ruptures are studied, and the degree of damage of sandstone specimens at the same loading rate decreases with the increase of water content, which shows that the average particle size linearly decreases rapidly with the increase of water content. At last, the intrinsic mechanism of different water contents on the tensile strength of sandstone was revealed by scanning electron microscopy. If the specimen has a relatively high water content, the microstructures become compact as internal kaolin and other components absorb water and swell, and this also causes the failure mode at high strain rate to change from ductile failure to typical brittle failure.

Data Availability

All the data of the pictures and tables used to support the findings of this study are included within the article, and they are all open data.

Conflicts of Interest

The authors declare that they have no conflicts of interest.

Acknowledgments

Financial support for this work was provided by the National Key Research and Development Program of China (2016YFC0501103) and the National Natural Science Foundation (51574222, 51704281, and U1803118).

References

- [1] Z. Sha, H. Pu, M. Li et al., "Experimental study on the creep characteristics of coal measures sandstone under seepage action," *Processes*, vol. 6, no. 8, p. 110, 2018.
- [2] D. Ma, M. Rezaia, H.-S. Yu, and H.-B. Bai, "Variations of hydraulic properties of granular sandstones during water inrush: effect of small particle migration," *Engineering Geology*, vol. 217, pp. 61–70, 2017.
- [3] Y. Lu and L. Wang, "Numerical simulation of mining-induced fracture evolution and water flow in coal seam floor above a confined aquifer," *Computers and Geotechnics*, vol. 67, pp. 157–171, 2015.
- [4] W. Sun, W. Zhou, and J. Jiao, "Hydrogeological classification and water inrush accidents in China's coal mines," *Mine Water and the Environment*, vol. 35, no. 2, pp. 214–220, 2016.
- [5] L. Pang, Q. Zhang, T. Wang, D. C. Lin, and L. Cheng, "Influence of laneway support spacing on methane/air explosion shock wave," *Safety Science*, vol. 50, no. 1, pp. 83–89, 2012.
- [6] C.-P. Lu, L.-M. Dou, X.-R. Wu, and Y.-S. Xie, "Case study of blast-induced shock wave propagation in coal and rock," *International Journal of Rock Mechanics and Mining Sciences*, vol. 47, no. 6, pp. 1046–1054, 2010.
- [7] J. C. Wang, F. X. Jiang, X. J. Meng, X. Y. Wang, S. T. Zhu, and Y. Feng, "Mechanism of rock burst occurrence in specially thick coal seam with rock parting," *Rock Mechanics and Rock Engineering*, vol. 49, no. 5, pp. 1953–1965, 2016.
- [8] S. L. Gariano, M. T. Brunetti, G. Iovine et al., "Calibration and validation of rainfall thresholds for shallow landslide forecasting in Sicily, Southern Italy," *Geomorphology*, vol. 228, pp. 653–665, 2015.
- [9] H. Bai, D. Ma, and Z. Chen, "Mechanical behavior of groundwater seepage in karst collapse pillars," *Engineering Geology*, vol. 164, pp. 101–106, 2013.
- [10] X. Lu, W. Zhou, X. Ding, X. Shi, B. Luan, and M. Li, "Ensemble learning regression for estimating unconfined compressive strength of cemented paste backfill," *IEEE Access*, vol. 7, pp. 72125–72133, 2019.
- [11] S. Wang, H. M. Li, W. Wang, and D. Y. Li, "Experimental study on mechanical behavior and energy dissipation of anthracite coal in natural and forced water-saturation states under triaxial loading," *Arabian Journal of Geosciences*, vol. 11, no. 21, p. 668, 2018.
- [12] H. L. Stück, T. Platz, A. Müller, and S. Siegesmund, "Natural stones of the Saale-Unstrut region (Germany): petrography and weathering phenomena," *Environmental Earth Sciences*, vol. 77, no. 8, p. 300, 2018.
- [13] X. G. Zhao, Z. Zhao, Z. Guo et al., "Influence of thermal treatment on the thermal conductivity of Beishan granite," *Rock Mechanics and Rock Engineering*, vol. 51, no. 7, pp. 2055–2074, 2018.
- [14] Z. A. Erguler and R. Ulusay, "Water-induced variations in mechanical properties of clay-bearing rocks," *International Journal of Rock Mechanics and Mining Sciences*, vol. 46, no. 2, pp. 355–370, 2009.
- [15] S. Tang, "The effects of water on the strength of black sandstone in a brittle regime," *Engineering Geology*, vol. 239, pp. 167–178, 2018.
- [16] J. F. Liu and H. Z. Zhang, "Water content influence on properties of red-layers in Guangzhou Metro line, China," *Advances in Materials Science and Engineering*, vol. 2017, Article ID 4808909, 12 pages, 2017.
- [17] Y. C. Yang, J. W. Zhou, F. G. Xu, and H. G. Xing, "An experimental study on the water-induced strength reduction in Zigong argillaceous siltstone with different degree of weathering," *Advances in Materials Science and Engineering*, vol. 2016, Article ID 4956986, 12 pages, 2016.
- [18] S.-Q. Yang, M. Chen, H.-W. Jing, K.-F. Chen, and B. Meng, "A case study on large deformation failure mechanism of deep soft rock roadway in Xin'An coal mine, China," *Engineering Geology*, vol. 217, pp. 89–101, 2017.
- [19] K. Hashiba, T. Okada, K. Tani et al., "Literature survey and experimental study on the direct tension test on rocks," *Geotechnical Testing Journal*, vol. 40, no. 2, Article ID 20160201, 2017.
- [20] D. Cen and D. Huang, "Direct shear tests of sandstone under constant normal tensile stress condition using a simple auxiliary device," *Rock Mechanics and Rock Engineering*, vol. 50, no. 6, pp. 1425–1438, 2017.
- [21] F. Dai and K. Xia, "Loading rate dependence of tensile strength anisotropy of Barre granite," *Pure and Applied Geophysics*, vol. 167, no. 11, pp. 1419–1432, 2010.
- [22] X. Li, T. Zhou, and D. Li, "Dynamic strength and fracturing behavior of single-flawed prismatic marble specimens under impact loading with a split-Hopkinson pressure bar," *Rock*

- Mechanics and Rock Engineering*, vol. 50, no. 1, pp. 29–44, 2017.
- [23] Q. B. Zhang and J. Zhao, “A review of dynamic experimental techniques and mechanical behaviour of rock materials,” *Rock Mechanics and Rock Engineering*, vol. 47, no. 4, pp. 1411–1478, 2014.
- [24] M. Li, X. Mao, L. Cao, H. Pu, R. Mao, and A. Lu, “Effects of thermal treatment on the dynamic mechanical properties of coal measures sandstone,” *Rock Mechanics and Rock Engineering*, vol. 49, no. 9, pp. 3525–3539, 2016.
- [25] T. Yin, L. Bai, X. Li, X. Li, and S. Zhang, “Effect of thermal treatment on the mode I fracture toughness of granite under dynamic and static coupling load,” *Engineering Fracture Mechanics*, vol. 199, pp. 143–158, 2018.
- [26] M. Li, X. Mao, H. Pu, Y. Chen, Y. Wu, and L. Zhang, “Effects of heating rate on the dynamic tensile mechanical properties of coal sandstone during thermal treatment,” *Shock and Vibration*, vol. 2017, Article ID 4137805, 11 pages, 2017.
- [27] Y. Lin, K. P. Zhou, R. G. Gao, J. L. Li, and J. Zhang, “Influence of chemical corrosion on pore structure and mechanical properties of sandstone,” *Geofluids*, vol. 2019, Article ID 7320536, 15 pages, 2019.
- [28] P. Wang, T. Yin, X. Li, S. Zhang, and L. Bai, “Dynamic properties of thermally treated granite subjected to cyclic impact loading,” *Rock Mechanics and Rock Engineering*, vol. 52, no. 4, pp. 991–1010, 2019.
- [29] Z. Zhou, X. Cai, W. Cao, X. Li, and C. Xiong, “Influence of water content on mechanical properties of rock in both saturation and drying processes,” *Rock Mechanics and Rock Engineering*, vol. 49, no. 8, pp. 3009–3025, 2016.



Hindawi

Submit your manuscripts at
www.hindawi.com

